Publication Year	2024
Acceptance in OA	2025-01-27T12:28:34Z
Title	Using the Ca ii Lines in T Tauri Stars to Infer the Abundance of Refractory Elements in the Innermost Disk Region
Authors	Micolta, Marbely, Calvet, Nuria, Thanathibodee, Thanawuth, Magris C., Gladis, Manara, Carlo F., VENUTI, LAURA, ALCALA', JUAN MANUEL, Herczeg, Gregory J.
Publisher's version (DOI)	10.3847/1538-4357/ad8884
Handle	http://hdl.handle.net/20.500.12386/35729
Journal	THE ASTROPHYSICAL JOURNAL
Volume	976

The Astrophysical Journal, 976:251 (15pp), 2024 December 1 https://doi.org/10.3847/1538-4357/ad8884

Using the Ca II Lines in T Tauri Stars to Infer the Abundance of Refractory Elements in the Innermost Disk Region

Marbely Micolta[1], Nuria Calvet[1], Thanawuth Thanathibodee[2], Gladis Magris C.[3], Carlo F. Manara[4], Laura Venuti[5], Juan Manuel Alcalá[6], and Gregory J. Herczeg[7]
[1] Department of Astronomy, University of Michigan, 1085 South University Avenue, Ann Arbor, MI 48109, USA; micoltam@umich.edu
[2] Department of Physics, Faculty of Science, Chulalongkorn University, 254 Phayathai Road, Pathumwan, Bangkok, 10330, Thailand
[3] Centro de Investigaciones de Astronomía "Francisco J. Duarte" CIDA, Av. Alberto Carnevali, Mérida 5101, Mérida, Venezuela
[4] European Southern Observatory, Karl-Schwarzschild-Strasse 2, 85748 Garching bei München, Germany
[5] SETI Institute, 339 Bernardo Avenue, Suite 200, Mountain View, CA 94043, USA
[6] INAF-Osservatorio Astronomico di Capodimonte, Salita Moiariello 16, 80131 Napoli, Italy
[7] Kavli Institute for Astronomy and Astrophysics, Peking University, Beijing 100871, People's Republic of China

Received 2024 June 14; revised 2024 October 16; accepted 2024 October 16; published 2024 November 27

Abstract

We present a study of the abundance of calcium in the innermost disk of 70 T Tauri stars in the star-forming regions of Chamaeleon I, Lupus, and Orion OB1b. We use calcium as a proxy for the refractory material that reaches the inner disk. We used magnetospheric accretion models to analyze the Ca II emission lines and estimate abundances in the accretion flows of the stars, which feed from the inner disks. We find Ca depletion in disks of all three star-forming regions, with 57% of the sample having $[\mathrm{Ca/H}] < -0.30$ relative to the solar abundance. All disks with cavities and/or substructures show depletion, consistent with trapping of refractories in pressure bumps. Significant Ca depletion ($[\mathrm{Ca/H}] < -0.30$) is also measured in 60% of full disks, although some of those disks may have hidden substructures or cavities. We find no correlation between Ca abundance and stellar or disk parameters except for the mass accretion rate onto the star. This could suggest that the inner and outer disks are decoupled, and that the mass accretion rate is related to a mass reservoir in the inner disk, while refractory depletion reflects phenomena in the outer disk related to the presence of structure and forming planets. Our results of refractory depletion and timescales for depletion are qualitatively consistent with expectations of dust growth and radial drift, including partitioning of elements, and constitute direct evidence that radial drift of solids locked in pebbles takes place in disks.

Unified Astronomy Thesaurus concepts: Protoplanetary disks (1300); Chemical abundances (224); T Tauri stars (1681)

1. Introduction

Protoplanetary disks are natural outcomes of the star formation process. During their lifetime, the initially gas-rich disks evolve by accreting mass onto the star and losing it through winds and photoevaporation (e.g., L. Hartmann et al. 2016). Concurrently, the mass locked in solids (dust) grows, settles, and drifts radially to the star, evolving into planetesimals and planets, terrestrial, or gas/ice giants (S. J. Weidenschilling 1997; F. Brauer et al. 2008; T. Birnstiel et al. 2012). As a consequence, the distribution of materials and the chemical composition in the disks differs from the ones of the parent cloud (e.g., K. I. Öberg et al. 2023).

The abundance of rocky (refractory) material, especially in the innermost gas disk, provides a crucial record of the processes that make the chemical composition change. Because refractories require the highest temperatures to sublimate, they remain in pebbles, millimeter-/centimeter-size solid particles, and are only affected by radial transport or trapping mechanisms in the disk (e.g., radial drift, pressure bumps, J. Drazkowska et al. 2022). One of these processes is planet formation, which not only removes the rocky material from the disk as they build their cores (e.g., M. Lambrechts & A. Johansen 2012; J. Drazkowska et al. 2022), but also blocks the inward drifting pebbles in pressure bumps (e.g., P. Pinilla et al. 2012; Z. Zhu et al. 2012; N. van der Marel et al. 2021), reducing the abundance of rocky material in the inner regions.

Metal depletion in young stars has been detected before; in particular, TW Hya studies in the ultraviolet revealed depletion of Fe and Si (G. J. Herczeg et al. 2002; J. H. Kastner et al. 2002; B. Stelzer & J. H. M. M. Schmitt 2004). In recent years, the idea that planet-induced disk pressure traps can cause the depletion of refractory elements in the accreting gas and the stars themselves has been explored both observationally by looking at the stellar abundances of Herbig Ae/Be stars (M. Kama et al. 2015; J. Guzmán-Díaz et al. 2023) and at the composition of gas accreting onto T Tauri Stars (TTSs; M. K. McClure 2019; M. K. McClure et al. 2020; M. Micolta et al. 2023) and brown dwarfs (K. France et al. 2010), and theoretically by exploring the effects of giant planet formation in disk evolution models (A. D. Schneider & B. Bitsch 2021a, 2021b; L. A. Hühn & B. Bitsch 2023).

In an effort to understand the behavior of refractory material in the inner disk and as a tracer of the disk structures, we adopted Ca as a proxy for this material and used the Ca II lines to measure the abundance of Ca to H. In accreting TTSs, the Ca II lines are the strongest emission lines of refractory elements present in the optical range and formed in the magnetospheric accretion flows—as evidenced by their higher line luminosities compared to nonaccreting stars, and profiles with high-velocity wings and redshifted absorption (e.g., R. Azevedo et al. 2006; K. Moto'oka & Y. Itoh 2013; M. Micolta et al. 2023)—which feed directly from the inner disks (L. Hartmann et al. 2016). In M. Micolta et al. (2023), a systematic analysis of the Ca II lines for TTSs of the Chamaeleon I cloud was performed, finding that the Ca II lines are much more sensitive to the accretion rate than the Hα line; the Ca II line profiles of the lowest accretors resemble the narrow profiles of nonaccreting stars, with the chromospheric contribution dominating the emission. The profile analysis also revealed the first hint toward the possibility of underabundance of Ca in the inner gas disks of TTSs, as some stars showed narrower Ca II profiles than expected given their broad and strong Hα lines, high values of the mass accretion rate, and predictions of magnetospheric accretion models.

Using an approximate indicator of the abundance of Ca based on the line luminosities, M. Micolta et al. (2023) found Ca depletion in all disks with cavities in their spectral energy distributions (SEDs), which are possibly opened by planets (C. Espaillat et al. 2014), consistent with the results of K. Moto'oka & Y. Itoh (2013), who found that the equivalent widths of the Ca II infrared triplet lines in TTSs with gaps were consistently one-tenth smaller than those without cavities. Furthermore, Ca depletion was found in some stars without signs of gaps in their SEDs. In all cases, we found that the level of depletion was too high to be explained by differences in the initial conditions. This suggests that Ca depletion in the inner disk could be a tracer for dust-trapping mechanisms that had yet to or would not open large enough gaps for them to show up in the SEDs. However, this analysis was performed for one star-forming region and the actual Ca abundance relative to H was calculated for only one star, T28. To obtain a broader view of this phenomenon and its possible origins, we need estimates of refractory abundances in the inner disk over a range of masses, ages, and environments.

Here, we report the Ca abundances for the inner disks of accreting TTSs in the regions of Chamaeleon I, Lupus, and the Orion OB1b association. We search for correlations between the Ca abundance of the inner disk and the properties of stars and disks. By quantitatively analyzing the Ca II lines formed in the accretion flows, we can access the bulk of the refractory material in the inner disk and by comparing our estimates with our sample properties, we aim to gain some insight into the processes responsible for the trapping of refractory elements.

This paper is organized as follows. In Section 2, we describe the observations and data sources. In Section 3, we describe the magnetospheric accretion models. In Section 4, we describe the methods used for the analysis of the observations and the application of the models to derive the Ca abundances. In Section 5, we present our results and explore the correlations with stellar and disk parameters. In Section 6, we discuss the implications of our results. Finally, in Section 7 we give our conclusions.

2. Observational Material

2.1. Classical TTSs

Our sample of accreting TTSs (classical TTSs (CTTSs)) consists of a subset of stars with flux-calibrated spectra from the X-shooter spectrograph (J. Vernet et al. 2011) at the ESO Very Large Telescope (VLT) for three different star-forming regions: Lupus (Lup; J. M. Alcalá et al. 2014, 2017), Chamaeleon I (ChaI; C. F. Manara et al. 2016, 2017b), and the Orion OB1b sub-association (Ori 1b, PENELLOPE VLT, Large Program, C. F. Manara et al. 2021). For ChaI and Lup, we adopted the stellar and accretion parameters of C. F. Manara et al. (2017a) and J. M. Alcalá et al. (2017), respectively, derived following the methods of C. F. Manara et al. (2013a), using the average distances for each cloud or subcloud. For Ori 1b, we adopted the stellar parameters from C. F. Manara et al. (2021), similarly carried out with the method of C. F. Manara et al. (2013a), but using the GAIA EDR3 (Gaia Collaboration et al. 2021) distances.

Table 1
Star-forming Regions

Region	d (pc)	Age (Myr)	N	References
Lup	150-200	3 ± 2	25	(1, 2, 3)
ChaI	160	3–5	37	(4, 5)
Ori 1b	400	5	8	(6)

Note. For each region, we report the average age found in literature, except for Lupus where we report the median age.

References. (1) J. M. Alcalá et al. (2014); (2) J. M. Alcalá et al. (2017); (3) A. Frasca et al. (2017); (4) K. L. Luhman (2007); (5) C. F. Manara et al. (2017b); (6) C. Briceño et al. (2019).

For the accretion properties of the Ori 1b targets, we used the revised values of C. V. Pittman et al. (2022) obtained from modeling near-ultraviolet and optical Hubble Space Telescope (HST) spectra, with the exception of CVSO 109 and CVSO 165. These are binary targets resolved by HST (C. R. Proffitt et al. 2021) but unresolved in the X-Shooter data; therefore, we used the parameters derived for the combined spectra in C. F. Manara et al. (2021). For each star, we adopt the same distance as the one used to derive the stellar and accretion parameters.

We focus on stars with Hα luminosities above the maximum luminosity observed for weak-line T Tauri stars (WTTSs) in our range of spectral types, that is $\log(L_{\mathrm{H}\alpha}/L_{\odot}) \geqslant -3.75$. With this criterion, we ensure that the emission is dominated by accretion and not the chromosphere, for which the analysis based on fluxes is applicable (e.g., M. Micolta et al. 2023). For the ChaI and Lup targets, we adopt the disk properties compiled in C. F. Manara et al. (2023), where the disk dust masses were obtained from the Atacama Large Millimeter/submillimeter Array (ALMA) Band 6 or 7 continuum data (I. Pascucci et al. 2016; M. Ansdell et al. 2016; F. Long et al. 2018; M. Ansdell et al. 2018), and the disk dust sizes were taken from N. Hendler et al. (2020). None of the Orion OB1b targets has millimeter imaging observations. Table 1 shows the properties of each region, and Table A1 shows the properties of each star included in our sample.

Table A1 includes information on the known disk morphology of the targets, grouped into three main categories: full disks (FDs; disks without known cavities or substructures), disks with substructures (SubS; disks with identified substructures by millimeter imaging), and transitional disks (TDs; disk with inner cavities inferred from SED modeling and confirmed by millimeter imaging). We note that most of our targets lack high spatial resolution observations. I. Pascucci et al. (2016) surveyed the ChaI region at a resolution of 0."6, resolving only cavities ⩾50 au. Similarly, most of the Lupus targets were imaged at 0."25 and only the cavities ⩾20 au have been resolved (M. Ansdell et al. 2016). Therefore, one cannot rule out the presence of smaller gaps or substructures in FDs; for instance, CR Cha appeared as an FD in I. Pascucci et al. (2016), but an outer ring was identified in S. Kim et al. (2020).

2.2. Weak-line TTSs

Given how magnetically active TTSs are, we need to consider the chromospheric contribution to properly compare the results of the magnetospheric accretion models with observations of CTTSs. For this purpose, we used X-shooter observations (C. F. Manara et al. 2013b, 2017a) of nonaccreting TTSs (WTTSs) in the same range of spectral types as our CTTS sample. The stellar properties are adopted from C. F. Manara et al. (2013b, 2017a) and the line fluxes from M. Micolta et al. (2023) (see Table A2).

3. Model

3.1. Magnetospheric Accretion Model

We use CV-multi (J. Muzerolle et al. 2001) to calculate the structure and emission of the magnetospheric accretion flows (L. Hartmann et al. 1994; J. Muzerolle et al. 1998, 2001). This framework assumes that the accretion flows follow the stellar magnetic field lines, which have a dipole geometry characterized by the inner radius (R_i) and the width at the base of the flow (Δr) in the disk. The density distribution is determined by the geometry and the mass accretion rate ($\dot{M}$). The models employ a semiempirical temperature distribution obtained by balancing a volumetric heating rate (r^{-3}) and an optically thin cooling law (L. Hartmann et al. 1994). It is parameterized by the maximum flow temperature ($T_{\rm max}$), constrained by the accretion rate, following the prescription of J. Muzerolle et al. (2001). The models use the extended Sobolev approximation to calculate mean intensities, which in turn are used to calculate the radiative rates in the statistical equilibrium equations. We adopt a 16-level hydrogen atom (J. Muzerolle et al. 2001) and a five-level calcium atom (M. Micolta et al. 2023) to calculate populations and optical depths. The abundance of Ca relative to H in the flows is left as a free parameter, and we cite it relative to the solar value ($\log(N_{\rm Ca}/N_{\rm H})_\odot = 6.31 \pm 0.04$, M. Asplund et al. 2005). Line profile calculations are performed using the ray-by-ray method for a given inclination angle i and assuming Voigt profiles (J. Muzerolle et al. 2001).

We calculated a large grid of magnetospheric models for five stars with spectral types covering the range of our CTTS sample. The stellar parameters were taken from the 3 Myr isochrone of the `PARSEC` evolutionary models (A. Bressan et al. 2012, Table 3), consistent with the average ages of our sample (see Table 1). For each model, we calculated profiles for the Balmer and Ca II lines, obtaining a total of 734,400 profiles combined for all the lines and stars. The full parameter space explored is described in Table 2, where for each combination of stellar and magnetospheric parameters, we calculated line profiles for abundances (by number) $(N_{\rm Ca}/N_{\rm H})/(N_{\rm Ca}/N_{\rm H})_\odot = 1, 0.5, 0.1, 0.01$ or equivalently [Ca/H][8] $= 0, -0.3, -1, -2$.

3.2. Model's Grid Reduction

After creating the grid of models, we found combinations of parameters do not reproduce line profiles comparable to observations, i.e., the parameters generate line profiles with Balmer lines fully in absorption or dominated by redshifted absorption, which do not correspond to the definition of the T Tauri class (G. H. Herbig & N. Kameswara Rao 1972). To properly identify all the combinations of parameters that result in this type of profile across the extensive grid, we evaluated the shape of the profiles by comparing the flux above and below the continuum for each line, obtaining that models reproduce realistic line profiles if $\log(F_{\rm H\alpha}) > 6.5$ and $\log(F_{\rm H\beta}) > 6.5$, where F is the line flux above the continuum in erg $\rm s^{-1}\,cm^{1}\,Hz^{-1}$ at the stellar surface, and we use this as our selection criterion to find the final models used when comparing with observations.

Table 2
Magnetospheric Parameter Space of the Models

Parameter	Min	Max	Step
SpT	M5	K2	2[a]
$\log \dot{M}$ ($M_\odot$ yr^{-1})	−10.0	−7.0	0.25
$T_{\rm max}$ (K)	6500	14,000	500
R_i ($R_\star$)	2.0	6.0	0.5
Δr ($R_\star$)	0.5	2.0	0.5
i (deg)	15	75	15
[Ca/H]	−2	0	…

Note.
[a] The last step made in SpT was three subclasses to better match the observations range.

4. Methods

To estimate the abundance of Ca in our targets, we focused on two lines: Hα and Ca II K. The Hα line traces the bulk of the gas, probing the accretion rate of the star (e.g., L. Hartmann et al. 2016). The Ca II K line is the strongest of the Ca II lines, without contamination from nearby hydrogen lines or significant photospheric contribution, so it can probe the depletion of Ca with fewer uncertainties (M. Micolta et al. 2023).

4.1. Line Fluxes and Luminosities

For ChaI stars and WTTSs, we used the fluxes reported in M. Micolta et al. (2023). For the Lupus and OB1b stars, we followed the same methods and calculated the fluxes of the Hα and Ca II K lines by integrating the continuum-subtracted line profiles corrected for extinction. The contribution of the photosphere for early K stars was removed by subtracting synthetic BT-Settl spectra (F. Allard et al. 2012; I. Baraffe et al. 2015). For a given star, we used a BT-Settl model with $T_{\rm eff}$ within 50 K of the star and a typical value of $\log g = 4.0$. Before subtraction, the model was convolved to the X-shooter resolution and rotationally broadened at the same rotational velocity ($v \sin i$) as the object. We used $v \sin i$ values from A. Frasca et al. (2017) for Lupus and C. V. Pittman et al. (2022) for Orion OB1b.

To determine the line fluxes, we calculated three independent measurements per line corresponding to the lowest, highest, and middle positions of the local continuum depending on the local noise level of the spectra. Subsequently, the flux and its error were calculated as the average and standard deviation of the three independent measurements, respectively. All fluxes and their errors are provided in Tables A1 and A2 for CTTSs and WTTSs, respectively. The luminosity of the

---

[8] $[{\rm Ca/H}] = \log(N_{\rm Ca}/N_{\rm H}) - \log(N_{\rm Ca}/N_{\rm H})_\odot$, where N refers to the abundances by number.

Table 3
Stellar Parameter Space of the Models

SpT	$T_{\rm eff}$ (K)	R ($R_\odot$)	M ($M_\odot$)
K2	4900	1.92	1.43
K5	4350	1.52	0.87
K7	4060	1.45	0.73
M1	3705	1.43	0.61
M3	3415	1.33	0.47
M5	3125	1.17	0.31

emission lines follows as $L_{\rm line} = 4\pi d^2 F_{\rm line}$ where d is the distance to the star (see Table A1).

To include the contribution of the chromosphere to the line luminosities of the models, we added the line luminosities of the WTTSs of the same spectral type to those of the models.

4.2. Ca Abundances

To estimate the abundance of Ca, we compared the measured $L_{\rm Ca\,II\,K}/L_{\rm H\alpha}$ values with those that would be expected from magnetospheric accretion models at the mass accretion rate $\dot{M}$ of each source. The mass accretion rate traces the density of the accretion flows, that is, the amount of material that falls onto the star, and it is known to be well correlated with $L_{\rm H\alpha}$ (L. Ingleby et al. 2013; J. M. Alcalá et al. 2014; M. Micolta et al. 2023). The $\dot{M}$ values for our targets were measured independently of this work from the UV excess (J. M. Alcalá et al. 2017; C. F. Manara et al. 2017a, 2021; C. V. Pittman et al. 2022). For a star depleted in Ca, $L_{\rm Ca\,II\,K}$ will be less than expected for its accretion rate (M. Micolta et al. 2023); therefore, the $L_{\rm Ca\,II\,K}/L_{\rm H\alpha}$ ratio will also be smaller than expected for its $\dot{M}$. In the following paragraphs, we describe how we calculated the Ca abundance for our targets.

We calculated the line luminosities of the models using the fluxes and radii of the model star (Table 3). For each of the models, we added line luminosities of a WTTS of the same spectral type to include the chromospheric level. Then, we took all the models with the same Ca abundance and mass accretion rate and calculated the median, 16th, and 84th quartiles of the $L_{\rm Ca\,II\,K}/L_{\rm H\alpha}$. This characterizes the behavior of $L_{\rm Ca\,II\,K}/L_{\rm H\alpha}$ with respect to the accretion rate for each value of [Ca/H].

To obtain a continuous behavior along the models, we interpolated between the median of the line ratio for each abundance of Ca, including the quartiles for the edges, generating a 3D piecewise interpolant between the $L_{\rm Ca\,II\,K}/L_{\rm H\alpha}$ ratio, the accretion rate, and the [Ca/H] values of the models. The color grid in Figure 1 shows the overall resulting behavior of the Ca abundance in the $L_{\rm Ca\,II\,K}/L_{\rm H\alpha}$ ratio versus the log $\dot{M}$ diagram; purple represents solar values, with depletion increasing toward red. Solid black lines represent the median value for each abundance; the dashed lines are the 16th and 84th quartiles for the lowest and highest abundance values, respectively. For comparison, we applied the same steps to the models without the chromospheric contribution, which is shown as the grayed-out region in Figure 1.

In addition to the models, we show the measured $L_{\rm Ca\,II\,K}/L_{\rm H\alpha}$ values for our sample with respect to log $\dot{M}$. The color of each point indicates whether the disk is known to have gaps (TD, black), a substructure (SubS, gray), or whether it is smooth (FD, white), and the shape represents the star-forming region to which each point belongs. To estimate the Ca abundance for our observations, we applied the constructed interpolants for the median, 16th, and 84th percentiles of the models, using the measured line ratio and the independently obtained accretion rate. We adopted the average value of the three determinations as the Ca abundance and the standard deviation as the error resulting from the method. Given the coarse nature of this technique, the uncertainties are mainly driven by the method rather than by the intrinsic uncertainties of the stellar parameters. Only the intrinsic error of the accretion rate is non-negligible, so we include this uncertainty by estimating the standard deviation of three values, the mean Ca abundance, and the abundance if the star had the accretion rate plus or minus its uncertainty. The general uncertainty is calculated by adding in quadrature; final values and errors are reported in Table A3. We have three outliers, namely Sz118, T4, and CVSO 165. We discuss the possible reasons for this behavior in Section 6.1.

We emphasize that this is a coarse method for calculating abundances; however, it allows us to analyze a large sample in an efficient way. A refined estimate of the abundance values requires simultaneous detailed fitting of multiple line profiles; the general abundance estimates are anticipated to remain the same, while the uncertainties of each estimate will be minimized. This will be carried out in future work for targets of interest.

5. Results

Figure 2 shows the probability density of Ca abundance in Ori OB1b, Lupus, and Chamaeleon. In general, we find a wide range of Ca abundances in all three star-forming regions. The overall distribution is right-skewed, with 57% of the sample having abundances $(N_{\rm Ca}/N_{\rm H})/(N_{\rm Ca}/N_{\rm H})_\odot < 0.50$ or [Ca/H] = –0.30, relative to solar, suggesting that there is a tendency toward high Ca depletion values (low abundances) in CTTSs.

We explored the probability that the distributions of the three star-forming regions were sampled from populations with identical distributions by performing two-sample Kolmogorov–Smirnov (KS) tests, where the null hypothesis was that the two distributions were identical, $F(x) = G(x)$ for all x. The p-value gives the probability of obtaining the observed results, assuming that the null hypothesis is true. For the purposes of this work, we rejected the null hypothesis if the value p of the chosen statistic was <0.05 (5%).

We performed three KS tests using the full sample of each region: ChaI-Lup, ChaI-OB1b, and Lup-OB1b (Table 4). For the first two cases, we obtain p-values significantly above 5%, indicating that it is unlikely that the underlying abundance distributions of ChaI-Lup and ChaI-OB1b differ from each other. The p-value for the Lup-OB1b test suggests that the probability for the underlying distributions of Lup and OB1b are the same is ∼10%. Except for CVSO 165, which falls outside the parameter space of the models (see Section 6.1), all stars in our OB1b sample are depleted, with a maximum value of $(N_{\rm Ca}/N_{\rm H})/(N_{\rm Ca}/N_{\rm H})_\odot$ of 0.41 or [Ca/H] = –0.39. As OB1b is the oldest region and Lupus the youngest of the sample, this could indicate age-dependent depletion. However, we cannot reach a strong conclusion since the null hypothesis cannot be rejected, and also considering that the Ori 1b sample is small compared to those of ChaI and Lup. Therefore, we cannot rule out the possibility that the underlying distributions of the three regions coincide with each other. Larger samples of old populations are needed to provide a more definitive conclusion.

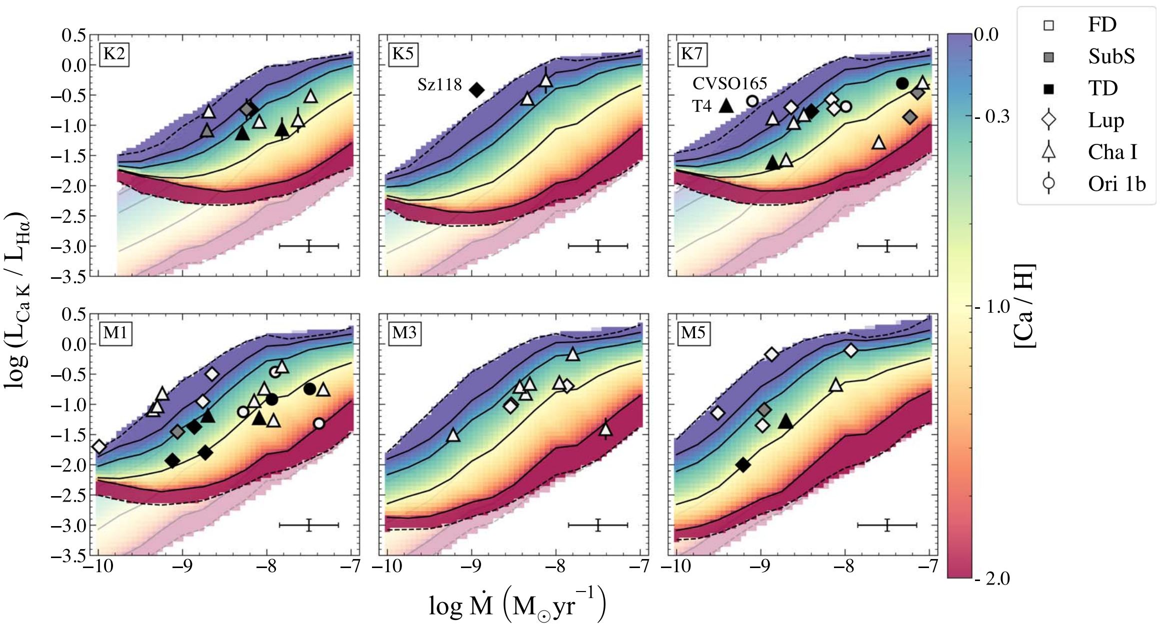

Figure 1. Comparison of $\log(L_{\mathrm{CaIIK}}/L_{\mathrm{H}\alpha})$ vs. accretion rate between magnetospheric accretion models (background) and observations (dots). Models are colored by [Ca/H], with purple representing solar abundance (1) and depletion increasing toward red. The grayed-out region represents the magnetospheric models without the contribution of the WTTS. Solid lines represent the median value for a given model abundance (1, 0.5, 0.1, 0.01) and dashed lines represent the 16th and 84th percentiles for the lowest and highest abundance values of the models, respectively. Typical uncertainties for observations are shown in the lower right corner.

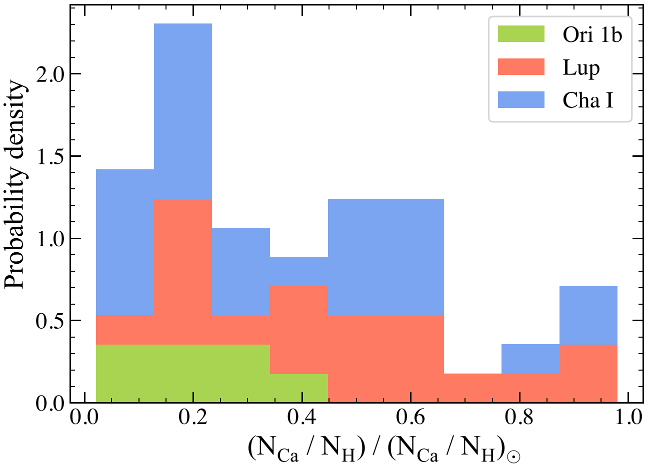

Figure 2. Probability density of the abundance by number, colored by star-forming region.

Table 4
$(N_{\mathrm{Ca}}/N_{\mathrm{H}})/(N_{\mathrm{Ca}}/N_{\mathrm{H}})_\odot$ by Regions' KS Test

Region	Statistic	*p*-value
ChaI-Lup	0.23	0.47
ChaI-Ori 1b	0.34	0.40
Lup-Ori 1b	0.48	0.10

5.1. Exploring Relationships between Ca Abundance and Stellar and Disk Parameters

In the next subsections, we explore correlations between the obtained Ca abundances and stellar parameters and disk structure for the whole sample. Additionally, we explore possible relationships between the abundance and disk properties for the ChaI and Lupus subsamples, for which disk parameters are known. We discuss the most significant insights in Section 6.

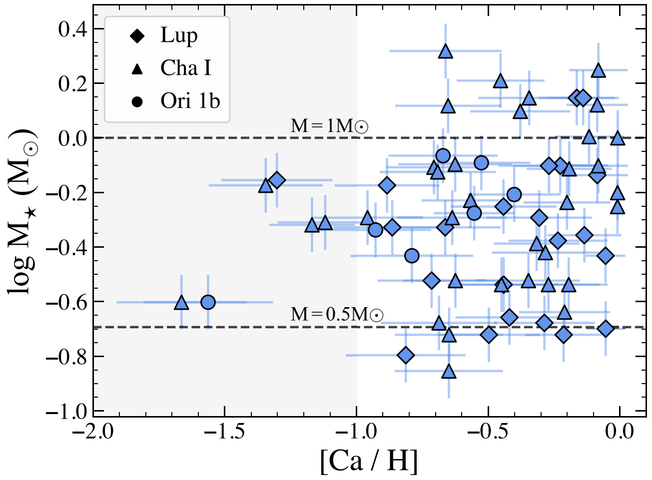

Figure 3. [Ca/H] vs. $M_\star$ The gray region highlights the [Ca/H] $\leqslant -1$ region, the minimum abundance we are able to detect for $M_\star > 1$. No relationship between the stellar mass and Ca abundance is found.

5.1.1. Relationship with Stellar Mass

Figure 3 shows the abundance of Ca ([Ca/H]) versus the stellar mass ($M_\star$). We note that for the $M_\star > 1 M_\odot$ sample, we do not find abundance values lower than -1 (gray area). At first glance, this would suggest that the lowest abundance values are found only in low-mass stars. However, biases in our estimates due to the small size of the high-mass sample and the detection limit imposed by the chromosphere probably contribute to the observed gap in abundances (see Section 6.2, see Figure 1).

We explored the statistical significance of the difference observed within the two mass groups ($M_\star \leqslant 1 M_\odot$ and

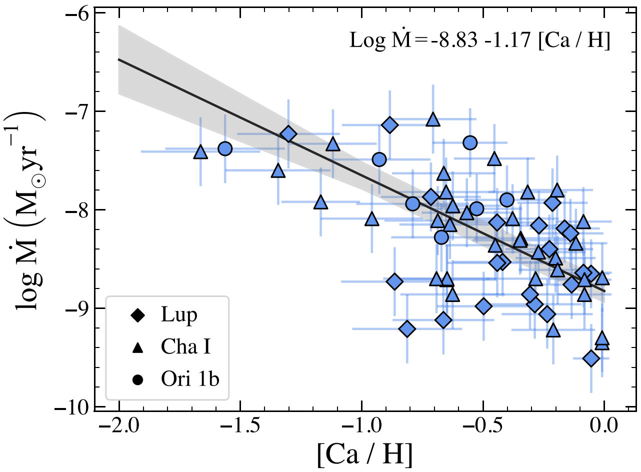

Figure 4. [Ca/H] vs. $\log(\dot{M})$. The black line represents the best fit from the Markov Chain Monte Carlo linear regression; our 1σ confidence intervals are shown in gray.

$M_\star > 1 M_\odot$), using a two-sample KS test, considering stars with $[\mathrm{Ca/H}] > -1$, to mitigate biases. We obtained a statistic of 0.33 with a p-value of 0.26, which provided evidence for the null hypothesis, that is, that the underlying distributions of the two mass samples were the same.

To test for a correlation between abundance and stellar mass, we calculate the Pearson correlation coefficient (hereafter the Pearson r test). In the cases where the p-value is <0.05, we reject the null hypothesis that there is no statistically significant relationship between the variables. We obtain a statistic of 0.17 with a p-value of 0.20; therefore, we do not find a correlation between Ca abundance and stellar mass.

5.1.2. Relationship with the Mass Accretion Rate

Figure 4 shows the mass accretion rate onto the star ($\dot{M}$) versus the Ca abundance for the three star-forming regions considered here. We explore the correlation between the two variables, calculating the Pearson correlation coefficient. We find a p-value lower than 5E-6% (see Table 5) and negative statistics (r), indicating that the data are anticorrelated, with higher abundances for lower accretion rates. As a follow-up, we then use the Bayesian linear regression method described in B. C. Kelly 2007 (implemented in the `linmix` Python package by Joshua E. Meyers) to fit the linear regression between [Ca/H] and $\log \dot{M}$ (Figure 4). This procedure takes into account the upper limits and intrinsic scatter in the data, fitting for $Y(X) = \alpha + \beta X$, where α and β are the intercept and slope, respectively. The best-fit parameters, together with the scatter of the relation (σ) and the correlation coefficient ($\hat{\rho}$), are reported in Table 5. We find $\log \dot{M} = -8.83\text{–}1.18$ [Ca/H]. We discuss the implications of this result in Section 6.4

5.1.3. Relationship with Disk Structure

Figure 5 shows the probability density of Ca abundance relative to H (by number), separating disks by their morphology: presence of gaps inferred from SEDs or imaging (red, TD), substructures inferred from imaging (green, SubS) or nondetection of structure (blue, FD) in each system. We explore possible differences between the underlying distributions by applying three KS tests: FD-TD, FD-Sub, and TD-Sub. In all cases, we obtain p-values significantly above 5% (see Table 6), indicating the possibility that the null hypothesis cannot be rejected and the underlying Ca abundance distributions coincide with each other. However, this result is affected by the small sample size of transitional and structured disks (17 and six stars, respectively) compared to the FD sample (48 stars). Moreover, the overall distributions, and therefore this result, are also subject to change as more cavities or substructures not yet identified in our objects are found. In the next paragraphs, we highlight the main takeaways.

The distribution plots show that all known disks with gaps (TD) for which we obtained an estimate [Ca/H] value show some degree of depletion with $(N_{\mathrm{Ca}}/N_{\mathrm{H}})/(N_{\mathrm{Ca}}/N_{\mathrm{H}})_\odot < 0.7$ or $[\mathrm{Ca/H}] < -0.15$ (black dashed line in Figure 5), as expected since cavities act as dust traps on the disk (e.g., P. Pinilla et al. 2012; Z. Zhu et al. 2012; N. van der Marel et al. 2021) resulting in lower refractory abundances in the innermost disk (e.g., L. A. Hühn & B. Bitsch 2023). SubS have a wide range of abundances, indicating that smaller substructures can also significantly impact the amount of refractory material reaching the star.

The two stars that show substructures in their disks and have $(N_{\mathrm{Ca}}/N_{\mathrm{H}})/(N_{\mathrm{Ca}}/N_{\mathrm{H}})_\odot > 0.7$ are Sz68 and CR Cha. Sz68 (HT Lup) is a triple stellar system with a projected separation of 25 au for the closest pair. The disk around Sz68 has an underlying spiral structure; however, the spirals are quite compact and appear to connect to the inner disk through a bar-like structure (N. T. Kurtovic et al. 2018). CR Cha has a gap at 90 au; inside this gap, the disk does not show evidence of any other substructure. Therefore, a possible explanation for these stars having high abundance values is that even when they have substructures, they do not interrupt the flow of the refractory material drifting toward the star. We note that our sample Sz71 (GW Lup) has a substructure similar to that of CR Cha, a smooth disk with a gap at 74 au (J. Huang et al. 2018) but appears to be depleted; however, for this particular target an unresolved inner cavity or dust trap was proposed to explain the observed column density ratio of $\mathrm{CO_2}$ to $\mathrm{H_2O}$ (S. L. Grant et al. 2023); this inner cavity could explain why GW Lup is depleted in Ca but not CR Cha.

What stands out in Figure 5 is the wide range of [Ca/H] values obtained for disks without known gaps/structures (FD), with abundances ranging from solar to −2. As discussed in Section 2.1, we cannot rule out the possibility that some systems may have gaps and substructures not properly identified. This is especially true for the ChaI sample, as only cavities $\gtrsim$50 au have been resolved (I. Pascucci et al. 2016) and lack detailed SED modeling. The analysis of Herbig Ae/Be stars made by M. Kama et al. (2015) identified two stars, HD 142666 and HD 144432, with significant subsolar abundances of refractory elements. These stars did not show indication of cavities in their SEDs (K. M. Maaskant et al. 2014); however, they showed radial gaps on the (sub)au scales in near-infrared interferometry (L. Chen et al. 2012; A. A. Schegerer et al. 2013; J. Menu et al. 2015). However, we see FDs with high depletion in the Lupus region, one of the better-characterized star-forming regions, suggesting that it is not just an issue of low spatial resolution but also a consequence of dust evolution on the disk.

5.1.4. Relationship with Disk Dust Mass and Radius

Submillimeter observations have been obtained for stars in ChaI and Lupus (e.g., M. Ansdell et al. 2016; I. Pascucci et al. 2016,

Table 5
[Ca/H] vs. Properties Statistical Tests

	Pearson r		Regression Parameters			
[Ca/H] versus	r	p-value	α	β	σ	$\hat{\rho}$
$\log M_\star$	0.17	0.20	…	…	…	…
$\log \dot{M}$	−0.58	5.46E-07	$-8.86^{+0.12}_{-0.12}$	$-1.30^{+0.24}_{-0.24}$	$0.07^{+0.05}_{-0.05}$	$-0.86^{+0.10}_{-0.10}$
$\log M_{\rm dust}$	−0.16	0.23	…	…	…	…
$\log R_{68}$	−0.17	0.33	…	…	…	…

Note. The regression parameters fit $Y(X) = \alpha + \beta X$, where α and β are the intercept and slope, respectively. (σ) is the scatter of the relation (σ) and ($\hat{\rho}$) the correlation coefficient.

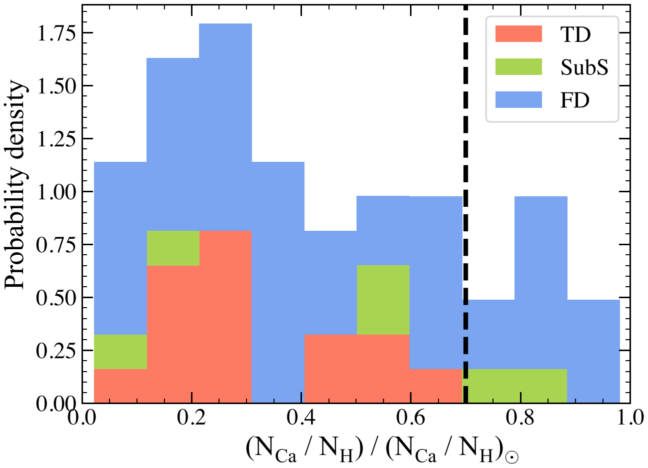

Figure 5. Probability density of abundance by number, colored according to the presence of gaps(red, TD), substructures (green, SubS), or absence of both (blue, FD) in each system. The black dashed lines represent $(N_{\rm Ca}/N_{\rm H})/(N_{\rm Ca}/N_{\rm H})_\odot = 0.7$.

Table 6
$(N_{\rm Ca}/N_{\rm H})/(N_{\rm Ca}/N_{\rm H})_\odot$ by Disk Structure KS Test

KS Test	Statistic	p-value
FD-TD	0.25	0.32
FD-Sub	0.23	0.45
TD-Sub	0.37	0.90

see Section 2.1), from which dust disk masses and radii have been inferred. Figure 6 shows the dust disk mass $M_{\rm dust}$ versus [Ca/H] for the ChaI and Lup stars with data from C. F. Manara et al. (2023, and references therein). We apply Pearson's r test and find that there is no statistically significant correlation between $M_{\rm dust}$ and [Ca/H] (p-value >0.05, see Table 5). However, we find that all six stars with [Ca/H] $\leqslant -1$, indicated in Figure 6 by the gray region, namely Sz98, T40, T28, VW Cha, and T49, have high $M_{\rm dust}$ values. None of the ChaI stars have predicted or confirmed cavities or substructures. However, Sz98 shows annular substructures in millimeter dust continuum emission imaging but no deficit in the SED, typical of TDs (D. Gasman et al. 2023). This also supports the notion that smaller substructures can also significantly impact the amount of refractory material reaching the star.

Finding the lowest abundances among the disks with high $M_{\rm dust}$ is consistent with the anticorrelation between Ca abundance and $\dot{M}$ (see Figure 4) since C. F. Manara et al. (2023) find a positive linear relationship between $M_{\rm dust}$ and $\dot{M}$ for young stars of multiple star-forming regions. Larger disk masses also allow for an easier and faster formation of giant planets (e.g., S. Savvidou & B. Bitsch 2023), which in turn can lead to the blocking of Ca in the outer disk becoming efficient at an earlier time when the accretion rate onto the star is still large. However, we note that some disks with high dust masses also have a high Ca abundance value, suggesting that there must be an additional parameter that determines the abundance.

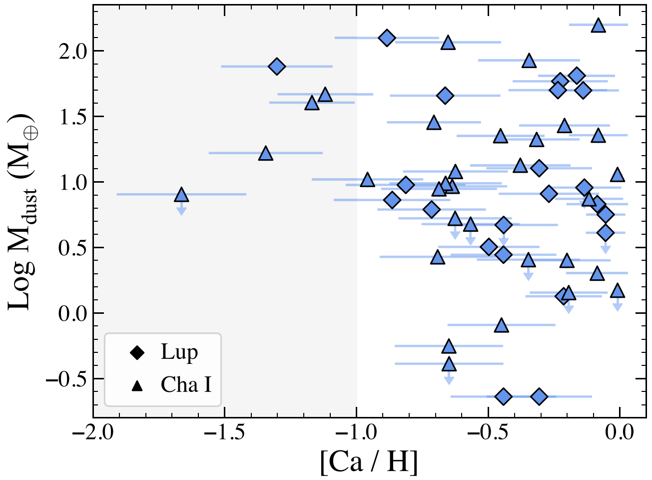

Figure 6. $M_{\rm dust}$ vs. [Ca/H]. Upper limits are indicated as arrows. No relationship between $M_{\rm dust}$ and [Ca/H] is found.

Next, we explore a possible correlation of the dust disk size. For this purpose, we use R_{68}, the radius containing 68% of the flux (N. Hendler et al. 2020; C. F. Manara et al. 2023). Figure 7 shows [Ca/H] versus R_{68}. We search for correlation within the variables by applying Pearson's r test. We find no correlation between [Ca/H] versus R_{68}, obtaining a Pearson r statistic of −0.17 with a p-value of 0.33 for the whole sample (see Table 5).

6. Discussion

6.1. Outliers

In Figure 1 we show that the observed ratios $\log(L_{\rm CaIIK}/L_{\rm H\alpha})$ when plotted against the mass accretion rates fall within the model predictions if the Ca abundance is allowed to vary. Three stars fall outside the model space in Figure 1: Sz118, T4, and CVSO 165. Here, we discuss possible reasons for the higher-than-expected $\log(L_{\rm CaIIK}/L_{\rm H\alpha})$ ratio of these stars, which the models do not reproduce. In principle, models with higher abundance could potentially explain these observations, but overabundances relative to solar are unexpected in this sample because (1) the star-forming regions are known to have solar abundances within uncertainties (e.g.,

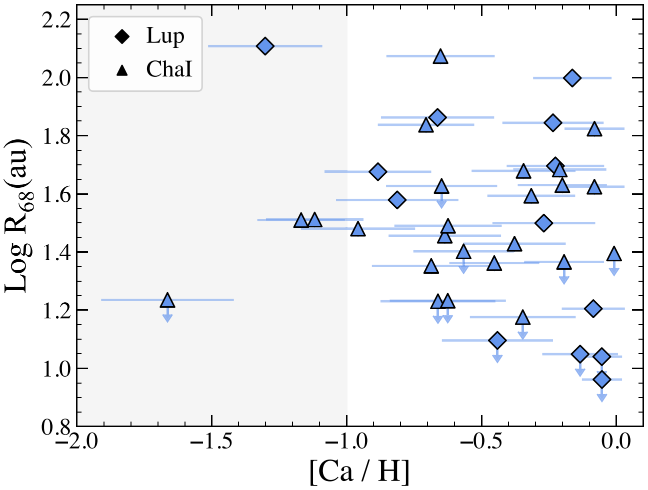

Figure 7. [Ca/H] vs. R$_{68}$. No relationship between R$_{68}$ and [Ca/H] is found.

N. C. Santos et al. 2008; V. D'Orazi et al. 2009; K. Biazzo et al. 2011a, 2011b; M. F. Nieva & N. Przybilla 2012; L. Spina et al. 2014); and (2) the estimated ages for these regions locate them after the initial period of enhanced abundances due to radial drift, predicted in partition models of dust evolution (L. A. Hühn & B. Bitsch 2023). Here, we discuss other possible reasons why our models do not reproduce these observations.

CVSO 165 is a binary system (C. R. Proffitt et al. 2021), but the X-Shooter spectra (C. F. Manara et al. 2021) correspond to the combined spectra of two stars, and so we used the stellar parameters derived in C. F. Manara et al. (2021) for the unresolved system. However, C. V. Pittman et al. (2022) separated both components and derived stellar and accretion properties for both stars. We note that for the more massive component (CVSO 165A), the spectral type falls within the uncertainties of the spectral type derived for the unresolved spectra, but the accretion rate is a factor of 10 higher. If we assume that the emission line ratio is dominated by the more massive component, then with the higher $\dot{M}$ and the observed $\log(L_{\rm CaIIK}/L_{\rm H\alpha})$, the star would be located inside the model space, with an abundance value of $(N_{\rm Ca}/N_{\rm H})/(N_{\rm Ca}/N_{\rm H})_{\odot} \sim 0.43$.

T4 is one of our lowest accretors and falls on the border of our threshold for a significant chromospheric contribution, i.e., when the luminosities of CTTSs and WTTSs are comparable ($\log(L_{\rm H\alpha}/L_{\odot}) \geqslant -3.75$). Its line profiles also resemble those of a WTTS; therefore, a flux-based analysis is not appropriate for this star. Instead, a detailed profile modeling is necessary (e.g., T. Thanathibodee et al. 2023); this will be addressed in future work.

Sz118 is a low accretor that shows multiple components in Hα: the profile is double-peaked with deep redshifted absorption that does not go below the continuum at low velocities ($\leqslant$150 km s^{-1}). We attribute this behavior to a highly complex composite magnetosphere (e.g., T. Thanathibodee et al. 2019). An accurate modeling of this type of profile is outside the scope of this paper.

6.2. Possible Sources of Bias

6.2.1. Sample Sizes

We note that our sample distribution is skewed toward low-mass stars, that is, the number of high-mass stars is small in comparison to that of low-mass stars. The bulk of our sample is formed by ChaI and Lup stars. Both regions have surveys of Class II objects with completion values of ~90% for TTSs, where the majority stars have SpT M3–M6 (J. M. Alcalá et al. 2017; C. F. Manara et al. 2017a; M. Micolta et al. 2023), an outcome of the initial mass function, which predicts an overdensity of low-mass stars compared to high-mass stars (e.g., N. Bastian et al. 2010). Our selection criterion, $\log(L_{\rm H\alpha}/L_{\odot}) \geqslant -3.75$ reduces the sample; however, it mainly affects the number of low-mass stars, rather than high-mass stars, as we are effectively excluding the lowest accretors (L. Hartmann et al. 2016).

6.2.2. Detection Limits Due to the Chromosphere

The chromosphere is an important component of the TTS spectra. In effect, the chromosphere acts like a *floor*, setting the minimum flux that we can detect for a given line, and its contribution increases with the effective temperature of the stars. Importantly, the Ca II lines are more sensitive to the chromosphere than Hα; therefore, the increase in Ca II K luminosity is steeper than the increase in the Hα luminosity as we move toward earlier spectral types. We quantified this effect by calculating the Pearson r test and linear regression of the line luminosities versus $T_{\rm eff}$ for the entire WTTS sample, following the same steps as in Section 5.1. The results are shown in Table 7. The slope of $\log L_{\rm CaIIK}$ versus $T_{\rm eff}$ is approximately two times the slope of $\log L_{\rm H\alpha}$ versus $T_{\rm eff}$. Consequently, the chromospheric contribution in $\log(L_{\rm CaIIK}/L_{\rm H\alpha})$ becomes important in the earlier spectral types as well, especially low accretion rates as the accretion component decreases. This effect can be seen in Figure 1, as the grayed-out region increases in area as we move from M5 to K2.

As a result, there is a minimum abundance that we are able to measure over the chromosphere. In particular, for K2 stars and $\log \dot{M} < -8.0$, we are unable to detect abundances [Ca/H] lower than −1, that is, $(N_{\rm Ca}/N_{\rm H})/(N_{\rm Ca}/N_{\rm H})_{\odot} < 0.1$, using only line fluxes. This, combined with the mass accretion rates of our high-mass sample, can partly explain why we do not see stars with $(N_{\rm Ca}/N_{\rm H})/(N_{\rm Ca}/N_{\rm H})_{\odot} < 0.20$ for this mass group (see Section 5.1.1 and Figure 3). For spectral types K5 to M1, we cannot estimate abundances lower than −1 if $\log \dot{M} < -8.75$. For M3–M5 stars, we should be able to detect abundances lower than −1 for accretion rates $\geqslant$−9.5 (see Figure 1).

6.3. Comparison with Predictions of Refractory Depletion

We estimated the abundance of refractory elements reaching the star using Ca as a proxy for refractory material. In the disk, Ca is locked in minerals with the highest condensation temperatures (K. Lodders 2003), so it should remain solid until it reaches the innermost disk, where the temperature is high enough for all material to be in gas. After the disk is truncated by interactions with the stellar magnetic field, gas falls onto the star along the stellar magnetic field lines, emitting characteristically broad spectral lines, which we have used to determine Ca abundances relative to H.

We have estimated abundances for 70 objects in three different star-forming regions, ChaI, Lupus, and Orion OB1b, covering 1–5 Myr, an interesting range of ages in which disk frequencies decrease from $\geqslant$60% to 10% (J. Hernández et al. 2007; Á. Ribas et al. 2014; A. J. W. Richert et al. 2018). In

Table 7
Line Luminosities vs. Effective Temperature for WTTSs

	Pearson r		Regression Parameters			
WTTS	r	p-value	α	β	σ	$\hat{\rho}$
$\log L_{\mathrm{CaIIK}}$	0.88	1.31E–09	$-43.24^{+4.42}_{-4.42}$	$10.67^{+1.23}_{-1.23}$	$0.91^{+0.05}_{-0.05}$	$0.16^{+0.07}_{-0.07}$
$\log L_{\mathrm{H}\alpha}$	0.75	8.44E–06	$-23.40^{+3.61}_{-3.61}$	$5.25^{+1.00}_{-1.00}$	$0.77^{+0.10}_{-0.10}$	$0.13^{+0.05}_{-0.05}$

Note. The regression parameters fit $Y(X) = \alpha + \beta X$, where α and β are the intercept and slope, respectively. (σ) is the scatter of the relation (σ) and ($\hat{\rho}$) the correlation coefficient.

addition to a range of ages, our samples cover a range of stellar masses, mass accretion rates, dust disk masses, and disk structures (Table A1). This diverse sample has allowed us to test for correlations with different parameters in order to explain the origin of the observed depletions.

Currently, we do not have detailed model predictions to compare our observed abundances. L. A. Hühn & B. Bitsch (2023) have developed partitioning models of dust evolution in disks, including grain growth, radial drift (T. Birnstiel et al. 2009), and separation of solids into chemical species. With this treatment, the abundances of elements locked into different minerals change as they drift in and sublimate into the gas phase when they reach temperatures higher than the condensation temperature of the mineral.

L. A. Hühn & B. Bitsch (2023) main emphasis is to make predictions for the abundance of elements on the stellar surface, taking into account the merging of the freshly accreted material with that of the star. In the range of mass and age of our sample, most stars have deep convection zones that are very efficient in mixing the accreted material with the stellar gas, rapidly erasing any chemical signature on the stellar surface (A. S. Jermyn & M. Kama 2018; M. Kunitomo et al. 2018). The predictions are applicable to earlier type stars, which lack sub-photospheric convective regions, and the accreted material reaching the surface does not get quickly mixed in.

L. A. Hühn & B. Bitsch (2023) do show the radial dependence of abundances as a function of age for three elements, C, O, and Fe. In their calculation, Fe is locked in minerals with condensation temperature ∼300–700 K, lower than that of the most refractory elements, ∼1500–1700 K, but still in the inner disk, so its behavior is representative of the refractory elements. The Fe behavior is clearly distinct from that of volatiles C and O. In the models shown in Figure 3 of L. A. Hühn & B. Bitsch (2023), the Fe abundance is enhanced relative to solar inside 1 au in the first ∼2 Myr, but quickly drops below solar beyond 3 Myr. The early overabundance is due to the arrival of the solid material locked in pebbles and moving inward faster than the gas; this material is accreted onto the star, after which the entire disk becomes depleted of Fe. This situation is in sharp contrast to the abundance of the volatiles, which stays above solar even beyond 10 Myr, and only gets depleted in the outer disk. In this case, the fraction of C and O locked in species of low condensation temperature (∼20–150 K) returns to the gas and takes longer than the refractories to reach the inner disk.

Our results are consistent with these findings. We find a significant level of depletion in the majority of the stars of the full sample, and moreover, all the disks in the older sample show depletion (see Figure 2, Ori 1b). This suggests that refractory depletion may be a general phenomenon in TTSs, most likely caused by dust evolution. In any event, our results in terms of depletion and timescales for depletion are consistent with expectations of dust growth and drift and constitute direct proof that radial drift of solids locked in pebbles takes place in disks.

The large dispersion in the Ca/H abundance found for each region—approximately of a given age—could be due to differences in the initial conditions, the viscosity parameter, and other factors that affect evolution. In fact, TTSs in a given population cover a wide range of disk properties, such as mass accretion rates, dust masses, and radii (L. Hartmann et al. 2016; A. M. Rilinger et al. 2023). Planet formation may be an additional factor that contributes to the large dispersion in a given population since the gaps opened by the planets can act as pressure traps (S. J. Paardekooper & G. Mellema 2006; P. Pinilla et al. 2012; Z. Zhu et al. 2012; N. van der Marel et al. 2021) and the planets themselves can capture solids (M. Lambrechts & A. Johansen 2012; A. Thiabaud et al. 2014; J. Drazkowska et al. 2022). The fact that all disks with detected gaps and structure, likely due to forming planets (e.g., S. Zhang et al. 2018), show depletion supports this statement.

Partitioning models of dust evolution, including refractory elements with high condensation temperature, covering a wide range of parameters, and allowing for planet formation, are needed for a more detailed comparison with our abundance estimations. This comparison will provide insight into dust evolution and planet formation models.

6.4. Dependence of [Ca/H] with Mass Accretion Rate

Our large sample has allowed us to search for dependences of refractory depletion with stellar, accretion, and disk parameters. We confirm our previous finding (M. Micolta et al. 2023) that refractory depletion is related to the structure of the disk, in the sense that all disks with large cavities identified in the SEDs and images show depletion, although the degree of depletion in structured disks varies. We found no correlation between refractory depletion and stellar mass, disk dust mass, or radius.

We find a significant correlation between Ca depletion and the mass accretion rate. This dependence is puzzling because the mass accretion rate depends on stellar mass as $\dot{M} \propto M^2$ (L. Hartmann et al. 2016, and references therein) and on dust disk mass (e.g., C. F. Manara et al. 2016, 2023; G. D. Mulders et al. 2017), and we find that depletion depends on $\dot{M}$, but does not correlate with either stellar or dust disk mass. We note that in C. F. Manara et al. (2023), the dependencies between stellar and dust disk mass become weak when mixing multiple regions; however, we found no correlation between $\dot{M}$ and these parameters when exploring the regions individually.

The abundance of Ca in relation to H is basically found by comparing the fluxes of the Ca II K line and Hα. In turn, the flux of Hα is correlated with the mass accretion rate (L. Ingleby et al. 2013). Therefore, the correlation between [Ca/H] and $\dot{M}$

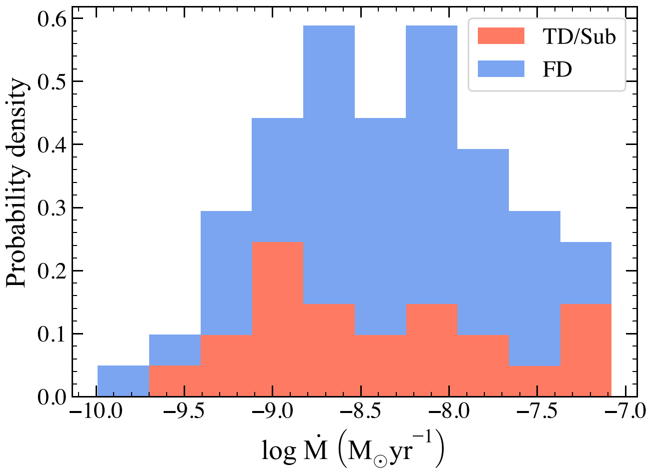

Figure 8. Distribution of abundance by number, colored according to the presence (red, TD/SubS) or absence of structure in the disk (blue, FD) in each system.

with slope ~ -1 could be understood if the abundance of solids reaching the inner disk was approximately constant, regardless of the abundance of gas reaching the inner disk, assuming that Ca is a proxy for solids.

We speculate that a possible explanation is that the inner and outer disks are decoupled and that the mass accretion rate mostly measures properties of the inner disk, while refractory depletion mostly reflects phenomena in the outer disks, related to the presence of structure and forming planets. To support this idea, we performed a two-sample KS test comparing the underlying mass accretion rate distributions of disks with and without structure (cavities or substructures), obtaining a statistic of 0.21 and a p-value of 0.46. This result indicates that it is unlikely that the underlying $\dot{M}$ distributions of structured and smooth disks differ from each other (see Figure 8).

The dichotomy between the inner and the outer disks has been explored before by proposing the existence of a mass reservoir in the inner disk, which would feed the accretion flows onto the star, while the outer disk evolves and may form planets. This mass reservoir could keep a relatively high-mass accretion rate onto the star, even when giant planets are forming in the disk and draining the gas flow from the outer disks (Z. Zhu et al. 2011); this, in turn, could explain the lack of massive disks accreting at very low accretion rates expected from planet population synthesis models, although the extent of the effects of accreting giant planets in the host star accretion rates is still debated (C. F. Manara et al. 2019; C. Bergez-Casalou et al. 2020, 2023). This mass reservoir could also reconcile the inner disk surface with that expected in the minimum mass solar nebula (L. Hartmann & J. Bae 2018), and could explain the strong accretors at old ages (L. Ingleby et al. 2014).

7. Summary and Conclusions

We used magnetospheric accretion models to analyze the VLT X-shooter spectra of 70 CTTSs from the star-forming regions of Chamaeleon I, Lupus, and Orion OB1b. We calculated Ca abundances relative to hydrogen for the sample and explored the connection between our results and stellar and disk properties from the literature. Here we summarize the main results:

1. We find a wide range of Ca abundances, with Ca depletion present in all three star-forming regions. The overall distribution of Ca abundances is skewed toward low [Ca/H] values (high values of depletion), with 57% of the sample having $[Ca/H] < -0.30$ relative to the solar. This indicates that refractory depletion is a very common result in CTTSs, most likely caused by dust/disk evolution.
2. The results of the two-sample KS test indicate that it is unlikely that the underlying abundance distributions between ChaI-Lup and ChaI-Ori 1b differ from each other, while the underlying distributions of Lup and Ori 1b are likely different from each other. This could hint at the difference in abundance distribution with age; however, given the small size of the Ori 1b sample, we cannot rule out the possibility that the underlying distributions of three star-forming regions in this work are similar.
3. All TDs are depleted in calcium with $[Ca/H] < -0.15$. We find disks with known substructures in a wide range of abundance values, with CR Cha and Sz68 being the only structured disks with higher abundance. In both cases the inner disk is still connected to the outer parts, and we suggest that there is no trapping mechanism diminishing the flow of rocky material to the central stars in these cases.
4. We find ∼60% of the full disks also show significant Ca depletion, with $[Ca/H] < -0.30$. However, we cannot rule out the possibility of hidden substructures and/or cavities in these subsamples. This is especially true for ChaI, where most of the stars were observed at a resolution of $0\farcs6$, resolving only cavities $\geqslant 50$ au (I. Pascucci et al. 2016). However, we still find FDs with high depletion values in Lupus, suggesting that this result is not only due to a detection bias.
5. For the ChaI and Lup subsamples, no correlation is found between Ca abundance and stellar mass nor disk dust mass.
6. We find an anticorrelation between [Ca/H] and the mass accretion rate, with a slope of ~ -1. Since the mass accretion is directly related to the abundance of gas, mostly represented by H, the anticorrelation would seem to imply that the abundance of solids reaching the inner disk is approximately constant, while Hα scales with mass accretion rate, assuming that the Ca abundance is a proxy for the solids. A possibility for this to happen is that there is an additional contribution to the infalling gas from an inner disk reservoir such as a dead zone, implying a decoupling of the inner and outer disk.
7. Our results in terms of depletion and timescales for depletion are qualitatively consistent with the expectations of dust growth and radial drift, including partitioning of elements (L. A. Hühn & B. Bitsch 2023), and constitute direct proof that radial drift of solids locked in pebbles takes place in disks.

Acknowledgments

We thank Bertram Bitsch, Lee Hartmann, and Zhaohuan Zhu for enlightening conversations and suggestions. This work has been partially supported by NASA grant 80NSSC24K0151.

Based on observations collected at the European Southern Observatory under ESO programs 106.20Z8.002, 084.C-0269(A), 085.C-0238(A), 086.C-0173(A), 087.C-0244(A), 089.C-0143(A), 095.C-0134(A), 097.C-0349(A), 095.C-0378(A), 084.C-1095(A), funded by the European Union (ERC, WANDA, 101039452). Views and opinions expressed are, however, those of the author(s) only and do not necessarily reflect those of the European Union or the European Research Council Executive Agency. Neither the European Union nor the granting authority can be held responsible for them.

J.M.A. acknowledges financial support from PRIN-MUR 2022 20228JPA3A "The path to star and planet formation in the JWST era (PATH)" funded by NextGeneration EU and by INAF-GoG 2022 "NIR-dark Accretion Outbursts in Massive Young stellar objects (NAOMY)." J.M.A. and C.F.M. acknowledge financial support from Large grant INAF 2022 "YSOs Outflows, Disks and Accretion: toward a global framework for the evolution of planet forming systems (YODA)."

The authors also acknowledge the referee for useful comments which improved the original manuscript.

Software: `Astropy` (Astropy Collaboration et al. 2013, 2018), `PyAstronomy` (S. Czesla et al. 2019), `Eniric` (J. Neal & P. Figueira 2019), `Scipy` (P. Virtanen et al. 2020), `Linmix` (J. Meyers 2015).

Appendix
Tables

This appendix contains Tables A1–A3 with TTS properties used in the analysis of this work.

Table A1
Stellar Parameters for Our CTTS Sample

Name	2MASS	SpT	T_{eff} (K)	A_V	M ($M_\odot$)	R ($R_\odot$)	$\log \dot{M}$	d (pc)	M_{dust} (1) ($M_\oplus$)	R_{68} (1) (au)	Disk
ChaI (2)											
CHX18N	J11114632−7620092	K2	4900.0	0.8	1.25	1.41	−8.09	160.0	13.39	26.8254	FD (r^a)
CHXR 47	J11103801−7732399	K4	4590.0	3.9	1.32	2.18	−8.12	160.0	2.01	⋯	FD (ur^a)
CR Cha	J10590699−7701404	K0	5110.0	1.3	1.77	2.3	−8.71	160.0	157.11	66.672	SubS^b
CS Cha	J11022491−7733357	K2	4900.0	0.8	1.4	1.67	−8.29	160.0	84.4	47.75	TD^c_c
CW Cha	J11123092−7644241	M0.5	3780.0	2.1	0.59	0.989	−8.03	160.0	4.76	<25.2525	FD (ur^a)
ESO-Ha-562	J11080297−7738425	M1	3705.0	3.4	0.56	0.841	−9.24	160.0	38.23	⋯	FD (r^a)
⋯	J11085367−7521359	M1	3705.0	1.5	0.51	1.06	−8.15	160.0	9.25	28.5	FD (r^a)
⋯	J11432669–7804454	M5.5	3060.0	0.4	0.14	1.07	−8.71	160.0	<0.56	⋯	FD (r^a)
Sz Cha	J10581677−7717170	K2	4900.0	1.3	1.31	1.5	−7.82	160.0	116	118.42	TD^c_c
Sz18	J11071915−7603048	M2	3560.0	1.3	0.38	1.34	−8.7	160.0	⋯	⋯	TD^d_u
Sz19	J11072074−7738073	K0	5110.0	1.5	2.08	2.88	−7.63	160.0	9.75	<17.0091	FD (r^a)
Sz22	J11075792−7738449	K5	4350.0	3.2	1.01	1.26	−8.34	160.0	7.42	⋯	FD (r^a)
Sz27	J11083905−7716042	K7	4060.0	2.9	0.8	1.16	−8.86	160.0	5.27	<17.082	TD^d_u
Sz32	J11095340−7634255	K7	4060.0	4.3	0.78	1.4	−7.08	160.0	28.46	68.76	FD (r^a)
Sz33	J11095407−7629253	M1	3705.0	1.8	0.56	0.805	−9.35	160.0	11.4	⋯	FD (r^a)
Sz37	J11104959−7717517	M2	3560.0	2.7	0.41	1.02	−7.82	160.0	21.07	39.2049	FD (r^a)
Sz45	J11173700−7704381	M0.5	3780.0	0.7	0.51	1.51	−8.09	160.0	10.44	30.2208	TD^d_u
T10	J11004022−7619280	M4	3270.0	1.1	0.23	0.985	−9.22	160.0	26.92	48.2525	FD (r^a)
T12	J11025504−7721508	M4.5	3200.0	0.8	0.19	1.26	−8.7	160.0	0.41	<42.366	TD^e_u
T16	J11045701−7715569	M3	3415.0	4.9	0.29	1.51	−7.8	160.0	1.43	<23.2308	FD (ur^a)
T23	J11065906−7718535	M4.5	3200.0	1.7	0.21	1.84	−8.11	160.0	8.84	22.5024	FD (r^a)
T24	J11071206−7632232	M0	3850.0	1.5	0.58	1.42	−8.49	160.0	2.52	42.6514	FD (ur^a)
T27	J11072825−7652118	M3	3415.0	1.2	0.29	1.67	−8.36	160.0	0.81	⋯	FD (nd^a)
T28	J11074366−7739411	M1	3705.0	2.8	0.48	1.33	−7.92	160.0	40.22	32.3408	FD (r^a)
T3	J10555973−7724399	K7	4060.0	2.6	0.77	0.858	−8.61	160.0	2.28	20.1828	FD (r^a)
T3 B	J10555973−7724399	M3	3415.0	1.3	0.29	1.25	−8.43	160.0	2.28	20.1828	⋯
T30	J11075809−7742413	M3	3415.0	3.8	0.3	1.14	−8.31	160.0	2.55	<15.0016	FD (ur^a)
T33 B	J11081509−7733531	K0	5110.0	2.7	1.0	1.06	−8.69	160.0	78.27	63.03	⋯
T38	J11085464−7702129	M0.5	3780.0	1.9	0.63	0.841	−9.3	160.0	1.49	<24.83	FD (ur^a)
T4	J10563044−7711393	K7	4060.0	0.5	0.78	1.33	−9.41	160.0	<1.33	139.1621	TD^c_c
T40	J11092379−7623207	M0.5	3780.0	1.2	0.49	1.73	−7.33	160.0	46.58	32.4904	FD (r^a)
T46	J11100704−7629376	K7	4060.0	1.2	0.75	1.47	−8.7	160.0	2.68	⋯	FD (ur^a)
T48	J11105333−7634319	M3	3415.0	1.2	0.3	1.14	−7.96	160.0	12	30.9168	FD (r^a)
T49	J11113965−7620152	M3.5	3340.0	1.0	0.25	1.61	−7.41	160.0	8.03	<17.19	FD (ur^a)
T52	J11122772−7644223	K0	5110.0	1.0	1.62	2.04	−7.48	160.0	22.49	23.0112	FD (r^a)
TW Cha	J10590108−7722407	K7	4060.0	0.8	0.79	1.25	−8.86	160.0	22.7	42.1176	FD (r^a)
VW Cha	J11080148−7742288	K7	4060.0	1.9	0.67	2.59	−7.6	160.0	16.59	⋯	FD (ur^a)
Lup (3)											
RYLup	J15592838−4021513	K2	4900.0	0.4	1.4	1.79	−8.19	150.0	64.6	99.54	TD^c_c
SSTc2dJ160927	J16092697−3836269	M4.5	3200.0	2.2	0.19	1.1	−7.93	200.0	1.34	⋯	FD (ur^f)
SSTc2dJ161243	J16124373−3815031	M1	3705.0	0.8	0.44	1.91	−8.76	160.0	9.04	<11.1895	FD (r^f)
Sz110	J16085157−3903177	M4	3270.0	0.0	0.22	1.61	−8.53	200.0	5.49	15.749	FD (r^f)

Table A1
(Continued)

Name	2MASS	SpT	$T_{\rm eff}$ (K)	A_V	M ($M_\odot$)	R ($R_\odot$)	log $\dot{M}$	d (pc)	$M_{\rm dust\ (1)}$ ($M_\oplus$)	$\mathrm{R}_{68\ (1)}$ (au)	Disk
Sz111	J16085468−3937431	M1	3705.0	0.0	0.47	1.4	−9.12	200.0	45.44	72.8502	$\mathrm{TD}_{\rm c}^{\rm c}$
Sz113	J16085780−3902227	M4.5	3197.0	1.0	0.2	0.83	−8.87	200.0	8.1	12.8424	FD (r^f)
Sz114	J16090185−3905124	M4.8	3175.0	0.3	0.21	1.82	−8.96	200.0	30.61	42.3252	SubS^g
Sz123A	J16105158−3853137	M1	3705.0	1.25	0.51	1.1	−8.86	200.0	<0.23	⋯	$\mathrm{TD}_{\rm c}^{\rm c}$
Sz123A	J16105158−3853137	M1	3705.0	1.25	0.51	1.1	−8.86	200.0	12.7	⋯	$\mathrm{TD}_{\rm c}^{\rm c}$
Sz123B	J16105158−3853137	M2	3560.0	0.0	0.46	0.58	−9.99	200.0	12.7	⋯	FD (nd^f)
Sz129	J15591647−4157102	K7	4060.0	0.9	0.79	1.23	−8.4	150.0	58.49	49.6403	$\mathrm{TD}_{\rm c}^{\rm c}$
Sz66	J15392828−3446180	M3	3415.0	1.0	0.29	1.29	−8.54	150.0	4.69	<12.4736	FD (ur^f)
Sz68	J15451286−3417305	K2	4900.0	1.0	1.4	3.14	−8.24	150.0	49.8	⋯	SubS^g
Sz69	J15451741−3418283	M4.5	3197.0	0.0	0.2	0.97	−9.51	150.0	5.63	<9.1536	FD (r^f)
Sz71	J15464473−3430354	M1.5	3632.0	0.5	0.42	1.43	−9.06	150.0	50.06	69.84	SubS^g
Sz72	J15475062−3528353	M2	3560.0	0.75	0.37	1.29	−8.65	150.0	4.09	<10.9697	FD (r^f)
Sz73	J15475693−3514346	K7	4060.0	3.5	0.79	1.35	−8.16	150.0	8.11	31.564	FD (r^f)
Sz74	J15480523−3515526	M3.5	3342.0	1.5	0.3	3.13	−7.87	150.0	6.15	⋯	FD (r^f)
Sz81A	J15555030−3801329	M4.5	3200.0	0.0	0.19	1.54	−8.98	150.0	3.19	⋯	FD (ur^f)
Sz83	J15564230−3749154	K7	4060.0	0.0	0.67	2.39	−7.14	150.0	125.22	47.4	SubS^g
Sz88A	J16070061−3902194	M0	3850.0	0.25	0.56	1.61	−8.13	150.0	2.78	⋯	$\mathrm{TD}_{\rm c}^{\rm c}$
Sz88A	J16070061−3902194	M0	3850.0	0.25	0.56	1.61	−8.13	150.0	<0.23	⋯	FD (r^f)
Sz90	J16071007−3911033	K7	4060.0	1.8	0.73	1.64	−8.64	200.0	6.76	16.037	FD (r^f)
Sz91	J16071159−3903475	M1	3705.0	1.2	0.47	1.36	−8.73	200.0	7.27	⋯	$\mathrm{TD}_{\rm c}^{\rm c}$
Sz98	J16082249−3904464	K7	4060.0	1.0	0.7	3.2	−7.23	200.0	75.85	128.1414	SubS^i
OB1b (4)											
CVSO 104	J05320638−0111000	M0.5	3700.0	0.05	0.37	1.64	−7.94	360.7	⋯	⋯	$\mathrm{TD}_{\rm u}^{\rm h}$
CVSO 107	J05322578−0036533	K6	4020.0	1.16	0.53	1.97	−7.32	330.4	⋯	⋯	$\mathrm{TD}_{\rm u}^{\rm h}$
CVSO 109	J05323265−0113461	M0.5	3799.0	0.1	0.46	2.21	−7.49	400.0	⋯	⋯	$\mathrm{TD}_u^{e,h}$
CVSO 146	J05354600−0057522	M2	3490.0	0.28	0.86	1.25	−8.28	332.0	⋯	⋯	⋯
CVSO 165	J05390257−0120323	K6	4040.0	0.2	0.84	2.02	−9.1	400.0	⋯	⋯	⋯
CVSO 176	J05402414−0031213	M1	3849.0	1.44	0.25	3.26	−7.38	302.4	⋯	⋯	⋯
CVSO 58	J05292326−0125153	K7	3970.0	1.39	0.81	1.05	−7.99	349.0	⋯	⋯	⋯
CVSO 90	J05312062−0049197	M0.5	3700.0	0.92	0.62	0.84	−7.9	338.7	⋯	⋯	⋯

Notes. SSTc2dJ1609 and SSTc2dJ1612 full names are SSTc2dJ160927.0-383628 and SSTc2dJ161243.8-381503, respectively.

References. Disk parameters from (1) C. F. Manara et al. (2023) and references therein (see Section 2.1). Stellar properties from (2) (ChaI: C. F. Manara et al. (2016, 2017b)); (3) (Lup: J. M. Alcalá et al. 2014, 2017); (4) (OB1b: C. F. Manara et al. 2021; C. V. Pittman et al. 2022) Typical uncertainties in mass accretion rate are 0.35 dex and 0.42 dex for stars of the ChaI and Lup regions, respectively. For the stars of Ori 1b, the mass accretion rates have typical uncertainties of 0.016 dex, except CVSO 109 and CVSO 165, which have typical errors of 0.45 dex.

Disk Morphology:

FD: Full disks.

r: Disk resolved with millimeter imaging, no cavities or substructures detected (a: I. Pascucci et al. 2016, f: M. Ansdell et al. 2016).

ur: Disk unresolved with millimeter imaging (a: I. Pascucci et al. 2016, f: M. Ansdell et al. 2016).

nd: Nondetection of the disk with millimeter imaging (a: I. Pascucci et al. 2016, f: M. Ansdell et al. 2016).

SubS: Substructures detected with millimeter imaging, e.g., ring in the outer disk, spiral arms (b: S. Kim et al. 2020, g: S. M. Andrews et al. 2018, i: D. Gasman et al. 2023).

TD: Transitional disks.

TD_c: Transitional disks, cavities confirmed by millimeter imaging (c: N. van der Marel 2023).

TD_u: Transitional disks, cavities predicted by SED (d: P. Manoj et al. 2011, h: K. Maucó et al. 2018) or by Lyα line profile (e: N. Arulanantham et al. 2023), but not confirmed by millimeter imaging.

Table A2
Names, Stellar Parameters, and Line Fluxes for Our WTTS Sample

Name	SpT	d (pc)	$T_{\rm eff}$ (K)	L ($L_\odot$)	R ($R_\odot$)	F(Hα)	σ(Hα)	F(Ca II K)	σ(Ca II K)
HBC 407	K0	140.0	5110.0	0.36	0.76	24.1	11.5	29.2	14.9
PZ99 J160843.4–260216	K0.5	145.0	5050.0	1.38	1.53	221.0	65.7	456.0	123.0
RX J1515.8–3331	K0.5	150.0	5050.0	1.25	1.46	114.0	33.2	135.0	36.4
PZ99 J160550.5–253313	K1	145.0	5000.0	0.98	1.32	156.0	47.0	260.0	69.4
RX J0438.6+1546	K2	140.0	4900.0	0.95	1.35	186.0	32.9	151.0	25.7
RX J1547.7–4018	K3	150.0	4730.0	0.83	1.36	70.0	23.2	109.0	20.0
RX J1538.6–3916	K4	150.0	4590.0	0.61	1.23	82.1	20.3	108.0	16.9
TWA9A	K5	68.0	4350.0	0.25	0.872	205.0	18.1	125.0	7.31
RX J1543.1–3920	K6	150.0	4205.0	0.40	1.19	71.1	8.91	58.0	3.94
RX J1540.7–3756	K6	150.0	4205.0	0.39	1.18	59.8	9.36	54.9	3.75
SO879	K7	360.0	4060.0	0.51	1.45	24.5	1.88	13.0	0.526
TWA25	M0	54.0	3850.0	0.25	1.11	528.0	31.0	224.0	8.41
TWA14	M0.5	96.0	3780.0	0.15	0.897	157.0	4.81	37.9	1.07
TWA13B	M1	59.0	3705.0	0.20	1.08	302.0	20.3	144.0	5.07
TWA7	M2	28.0	3415.0	0.07	0.769	476.0	17.5	136.0	3.36
TWA2A	M2	47.0	3560.0	0.33	1.51	570.0	41.1	279.0	10.3
TWA15B	M2	111.0	3415.0	0.11	0.946	69.9	1.38	15.0	0.267
TWA9B	M3	68.0	3415.0	0.07	0.743	72.5	2.59	21.5	0.641
TWA15A	M3.5	111.0	3340.0	0.11	1.0	103.0	1.51	18.8	0.292
Sz94	M4	200.0	3270.0	0.17	1.3	27.3	0.84	7.12	0.197
SO797	M4.5	360.0	3200.0	0.06	0.763	1.79	0.05	0.302	0.007
SO641	M5	360.0	3125.0	0.03	0.586	1.21	0.03	0.169	0.004
Par-Lup3-2	M5	200.0	3125.0	0.18	1.44	10.7	0.38	1.3	0.079
SO999	M5.5	360.0	3060.0	0.05	0.815	2.03	0.04	0.211	0.005
SO925	M5.5	360.0	3060.0	0.03	0.57	0.83	0.02	0.085	0.002
LM 717	M6.5	160.0	2935.0	0.02	0.516	1.35	0.03	0.075	0.004

Note. Fluxes in units of 10^{-15}erg s^{-1} cm^{-2}

References. Stellar properties from C. F. Manara et al. (2013b, 2017a), fluxes from M. Micolta et al. (2023).

Table A3
Designations, Line Fluxes, and Ca Abundances for the TTSs in Our Sample

Name	2MASS	F (Hα)	σ (Hα)	F (Ca II K)	σ (Ca II K)	X[a]	σ (X)	[Ca/H]	σ ([Ca/H])
ChaI (1)									
CHX18N	J11114632–7620092	172.0	19.5	19.8	3.99	0.42	0.36	−0.38	0.27
CHXR 47	J11103801–7732399	77.5	34.0	43.4	10.5	0.82	0.3	−0.09	0.13
CR Cha	J10590699–7701404	1140.0	70.9	94.6	25.8	0.83	0.34	−0.08	0.15
CS Cha	J11022491–7733357	709.0	34.3	52.5	10.2	0.45	0.38	−0.34	0.27
CW Cha	J11123092–7644241	237.0	6.4	43.3	5.17	0.27	0.2	−0.57	0.24
ESO-Ha-562	J11080297–7738425	89.6	1.66	13.6	0.34	1.0[b]	…	0.0[b]	…
J11085367–7521359	J11085367–7521359	176.0	4.83	20.1	3.18	0.23	0.2	−0.64	0.28
J11432669–7804454	J11432669–7804454	45.3	0.77	2.35	0.13	0.22	0.2	−0.65	0.27
Sz Cha	J10581677–7717170	301.0	33.0	26.0	11.8	0.22	0.18	−0.65	0.25
Sz18	J11071915–7603048	45.8	2.86	2.99	0.2	0.52	0.43	−0.28	0.26
Sz19	J11072074–7738073	1180.0	105.0	144.0	78.4	0.22	0.18	−0.66	0.26
Sz22	J11075792–7738449	273.0	8.93	75.7	5.47	0.76	0.37	−0.12	0.17
Sz27	J11083905–7716042	191.0	6.13	4.62	0.47	0.24	0.2	−0.63	0.26
Sz32	J11095340–7634255	2350.0	39.8	1200.0	79.6	0.2	0.13	−0.71	0.21
Sz33	J11095407–7629253	25.5	1.36	2.06	0.17	0.98	0.03	−0.01	0.01
Sz37	J11104959–7717517	274.0	6.47	117.0	5.55	0.48	0.27	−0.32	0.19
Sz45	J11173700–7704381	272.0	6.35	16.2	2.08	0.11	0.11	−0.96	0.3
T10	J11004022–7619280	41.7	0.87	1.31	0.1	0.62	0.42	−0.21	0.22
T12	J11025504–7721508	33.6	0.77	1.79	0.14	0.22	0.2	−0.65	0.27
T16	J11045701–7715569	27.0	3.38	18.4	1.74	0.64	0.31	−0.19	0.17
T23	J11065906–7718535	140.0	2.29	29.7	0.61	0.21	0.18	−0.69	0.28
T24	J11071206–7632232	38.6	6.13	5.74	0.44	0.63	0.41	−0.2	0.22
T27	J11072825–7652118	68.1	3.33	10.3	0.73	0.36	0.35	−0.45	0.3

Table A3
(Continued)

Name	2MASS	F (Hα)	σ (Hα)	F (Ca II K)	σ (Ca II K)	X[a]	σ (X)	[Ca/H]	σ ([Ca/H])
T28	J11074366–7739411	312.0	7.6	17.0	1.22	0.07	0.04	−1.17	0.2
T3	J10555973–7724399	137.0	4.07	15.1	1.73	0.64	0.41	−0.19	0.21
T3 B	J10555973–7724399	32.9	1.82	6.47	0.58	0.54	0.45	−0.27	0.26
T30	J11075809–7742413	126.0	2.7	27.7	0.94	0.45	0.4	−0.35	0.28
T33 B	J11081509–7733531	276.0	15.9	47.0	11.6	0.98	0.03	−0.01	0.02
T38	J11085464–7702129	39.0	1.95	3.65	0.33	0.98	0.03	−0.01	0.01
T4	J10563044–7711393	25.0	3.38	5.28	0.24	…	…	…	…
T40	J11092379–7623207	471.0	15.7	83.5	13.3	0.08	0.05	−1.12	0.21
T46	J11100704–7629376	206.0	9.48	5.49	0.7	0.2	0.17	−0.69	0.27
T48	J11105333–7634319	396.0	3.44	91.0	1.87	0.24	0.19	−0.62	0.26
T49	J11113965–7620152	237.0	5.29	9.3	4.74	0.02	0.02	−1.66	0.28
T52	J11122772–7644223	3010.0	101.0	919.0	57.1	0.35	0.24	−0.45	0.22
TW Cha	J10590108–7722407	122.0	5.21	15.9	0.96	0.83	0.32	−0.08	0.14
VW Cha	J11080148–7742288	1130.0	32.0	59.0	4.3	0.05	0.04	−1.34	0.27
Lup									
RYLup	J15592838-4021513	239.0	39.3	44.5	13.5	0.69	0.38	−0.16	0.19
SSTc2dJ160927	J16092697-3836269	32.0	0.96	25.0	0.73	0.61	0.35	−0.21	0.2
SSTc2dJ161243	J16124373-3815031	48.2	4.11	5.37	0.32	0.73	0.4	−0.13	0.19
Sz110	J16085157-3903177	47.4	1.56	4.72	0.4	0.38	0.38	−0.42	0.3
Sz111	J16085468-3937431	114.0	2.69	1.33	0.17	0.22	0.19	−0.66	0.27
Sz113	J16085780-3902227	26.0	0.26	17.4	0.19	1.0[b]	…	0.0[b]	…
Sz114	J16090185-3905124	28.3	0.84	2.3	0.09	0.52	0.44	−0.29	0.27
Sz118	J16094864-3911169	64.1	7.82	24.5	1.79	…	…	…	…
Sz123A	J16105158-3853137	197.0	2.21	8.35	0.45	0.49	0.46	−0.31	0.28
Sz123B	J16105158-3853137	31.1	0.38	0.62	0.03	1.0[b]	…	0.0[b]	…
Sz129	J15591647-4157102	113.0	7.48	19.2	2.17	0.59	0.43	−0.23	0.24
Sz66	J15392828-3446180	66.0	2.12	6.07	0.44	0.36	0.36	−0.44	0.3
Sz68	J15451286-3417305	621.0	127.0	114.0	36.5	0.73	0.38	−0.14	0.18
Sz69	J15451741-3418283	73.4	0.46	5.27	0.06	0.88	0.29	−0.05	0.12
Sz71	J15464473-3430354	118.0	2.88	4.15	0.21	0.58	0.44	−0.24	0.25
Sz72	J15475062-3528353	178.0	2.81	56.3	0.55	0.88	0.29	−0.05	0.12
Sz73	J15475693-3514346	272.0	8.26	72.0	2.75	0.54	0.42	−0.27	0.25
Sz74	J15480523-3515526	111.0	7.94	22.3	1.12	0.19	0.17	−0.71	0.27
Sz81A	J15555030-3801329	32.4	0.89	1.45	0.05	0.32	0.37	−0.5	0.33
Sz83	J15564230-3749154	1700.0	28.4	593.0	16.8	0.13	0.12	−0.88	0.28
Sz84	J15580252-3736026	51.2	0.9	0.51	0.06	0.15	0.18	−0.81	0.34
Sz88A	J16070061-3902194	242.0	4.99	45.2	1.78	0.36	0.37	−0.44	0.3
Sz90	J16071007-3911033	60.8	6.53	12.0	1.07	0.82	0.37	−0.09	0.16
Sz91	J16071159-3903475	171.0	2.3	2.72	0.32	0.14	0.15	−0.86	0.33
Sz98	J16082249-3904464	425.0	27.9	58.0	5.74	0.05	0.04	−1.3	0.25
OB1b									
CVSO 104	J05320638-0111000	34.0	0.73	4.11	0.15	0.16	0.12	−0.79	0.23
CVSO 107	J05322578-0036533	30.7	2.24	15.1	1.13	0.28	0.12	−0.55	0.15
CVSO 109	J05323265-0113461	58.4	2.4	10.5	0.78	0.12	0.11	−0.93	0.29
CVSO 146	J05354600-0057522	44.9	2.84	3.36	0.22	0.21	0.13	−0.67	0.21
CVSO 165	J05390257-0120323	37.4	2.96	9.38	0.43	…	…	…	…
CVSO 176	J05402414-0031213	64.4	1.56	3.1	0.55	0.03	0.02	−1.56	0.25
CVSO 58	J05292326-0125153	54.0	2.38	11.0	1.05	0.3	0.16	−0.53	0.19
CVSO 90	J05312062-0049197	105.0	1.25	35.9	0.8	0.4	0.2	−0.4	0.18

Notes. (1) Fluxes from M. Micolta et al. (2023). Fluxes in units of 10^{-14} erg s^{-1} cm^{-2}.

[a] X refers to $(N_{\rm Ca}/N_{\rm H})/(N_{\rm Ca}/N_{\rm H})_\odot$, where N is the abundance by number.

[b] CTTSs fall at the edge of the model's parameter space.

ORCID iDs

Marbely Micolta https://orcid.org/0000-0001-8022-4378
Nuria Calvet https://orcid.org/0000-0002-3950-5386
Thanawuth Thanathibodee https://orcid.org/0000-0003-4507-1710
Gladis Magris C. https://orcid.org/0000-0003-1166-5123
Carlo F. Manara https://orcid.org/0000-0003-3562-262X
Laura Venuti https://orcid.org/0000-0002-4115-0318
Juan Manuel Alcalá https://orcid.org/0000-0001-8657-095X
Gregory J. Herczeg https://orcid.org/0000-0002-7154-6065

References

Alcalá, J. M., Manara, C. F., Natta, A., et al. 2017, A&A, 600, A20
Alcalá, J. M., Natta, A., Manara, C. F., et al. 2014, A&A, 561, A2
Allard, F., Homeier, D., & Freytag, B. 2012, RSPTA, 370, 2765
Andrews, S. M., Huang, J., Pérez, L. M., et al. 2018, ApJL, 869, L41
Ansdell, M., Williams, J. P., Trapman, L., et al. 2018, ApJ, 859, 21
Ansdell, M., Williams, J. P., van der Marel, N., et al. 2016, ApJ, 828, 46
Arulanantham, N., Gronke, M., Fiorellino, E., et al. 2023, ApJ, 944, 185
Asplund, M., Grevesse, N., & Sauval, A. J. 2005, in ASP Conf. Ser. 336, Cosmic Abundances as Records of Stellar Evolution and Nucleosynthesis, ed. I. Barnes, G. Thomas, & F. N. Bash (San Francisco, CA: ASP), 25
Astropy Collaboration, Price-Whelan, A. M., Sipőcz, B. M., et al. 2018, AJ, 156, 123
Astropy Collaboration, Robitaille, T. P., & Tollerud, E. J. 2013, A&A, 558, A33
Azevedo, R., Calvet, N., Hartmann, L., et al. 2006, A&A, 456, 225
Baraffe, I., Homeier, D., Allard, F., & Chabrier, G. 2015, A&A, 577, A42
Bastian, N., Covey, K. R., & Meyer, M. R. 2010, ARA&A, 48, 339
Bergez-Casalou, C., Bitsch, B., Pierens, A., Crida, A., & Raymond, S. N. 2020, A&A, 643, A133
Bergez-Casalou, C., Bitsch, B., & Raymond, S. N. 2023, A&A, 669, A129
Biazzo, K., Randich, S., & Palla, F. 2011a, A&A, 525, A35
Biazzo, K., Randich, S., Palla, F., & Briceño, C. 2011b, A&A, 530, A19
Birnstiel, T., Dullemond, C. P., & Brauer, F. 2009, A&A, 503, L5
Birnstiel, T., Klahr, H., & Ercolano, B. 2012, A&A, 539, A148
Brauer, F., Dullemond, C. P., & Henning, T. 2008, A&A, 480, 859
Bressan, A., Marigo, P., Girardi, L., et al. 2012, MNRAS, 427, 127
Briceño, C., Calvet, N., Hernández, J., et al. 2019, AJ, 157, 85
Chen, L., Kreplin, A., Wang, Y., et al. 2012, A&A, 541, A104
Czesla, S., Schröter, S., Schneider, C. P., et al. 2019, PyA: Python Astronomy-related Packages, Astrophysics Source Code Library, ascl:1906.010
D'Orazi, V., Randich, S., Flaccomio, E., et al. 2009, A&A, 501, 973
Drazkowska, J., Bitsch, B., Lambrechts, M., et al. 2023, in SP Conf. Ser. 534, Protostars and Planets VII, ed. S. Inutsuka et al. (San Francisco, CA: ASP), 717
Espaillat, C., Muzerolle, J., Najita, J., et al. 2014, in Protostars and Planets VI, ed. H. Beuther et al. (Tucson, AZ: Univ. of Arizona Press), 497
France, K., Linsky, J. L., Brown, A., Froning, C. S., & Béland, S. 2010, ApJ, 715, 596
Frasca, A., Biazzo, K., Alcalá, J. M., et al. 2017, A&A, 602, A33
Gaia Collaboration, Brown, A. G. A., Vallenari, A., et al. 2021, A&A, 649, A1
Gasman, D., van Dishoeck, E. F., Grant, S. L., et al. 2023, A&A, 679, A117
Grant, S. L., van Dishoeck, E. F., Tabone, B., et al. 2023, ApJL, 947, L6
Guzmán-Díaz, J., Montesinos, B., Mendigutía, I., et al. 2023, A&A, 671, A140
Hartmann, L., & Bae, J. 2018, MNRAS, 474, 88
Hartmann, L., Herczeg, G., & Calvet, N. 2016, ARA&A, 54, 135
Hartmann, L., Hewett, R., & Calvet, N. 1994, ApJ, 426, 669
Hendler, N., Pascucci, I., Pinilla, P., et al. 2020, ApJ, 895, 126
Herbig, G. H., & Kameswara Rao, N. 1972, ApJ, 174, 401
Herczeg, G. J., Linsky, J. L., Valenti, J. A., Johns-Krull, C. M., & Wood, B. E. 2002, ApJ, 572, 310
Hernández, J., Hartmann, L., Megeath, T., et al. 2007, ApJ, 662, 1067
Huang, J., Andrews, S. M., Dullemond, C. P., et al. 2018, ApJL, 869, L42
Hühn, L. A., & Bitsch, B. 2023, A&A, 676, A87
Ingleby, L., Calvet, N., Herczeg, G., et al. 2013, ApJ, 767, 112
Ingleby, L., Calvet, N., Hernández, J., et al. 2014, ApJ, 790, 47
Jermyn, A. S., & Kama, M. 2018, MNRAS, 476, 4418
Kama, M., Folsom, C. P., & Pinilla, P. 2015, A&A, 582, L10
Kastner, J. H., Huenemoerder, D. P., Schulz, N. S., Canizares, C. R., & Weintraub, D. A. 2002, ApJ, 567, 434
Kelly, B. C. 2007, ApJ, 665, 1489
Kim, S., Takahashi, S., Nomura, H., et al. 2020, ApJ, 888, 72
Kunitomo, M., Guillot, T., Ida, S., & Takeuchi, T. 2018, A&A, 618, A132
Kurtovic, N. T., Pérez, L. M., Benisty, M., et al. 2018, ApJL, 869, L44
Lambrechts, M., & Johansen, A. 2012, A&A, 544, A32
Lodders, K. 2003, ApJ, 591, 1220
Long, F., Herczeg, G. J., Pascucci, I., et al. 2018, ApJ, 863, 61
Luhman, K. L. 2007, ApJS, 173, 104
Maaskant, K. M., Min, M., Waters, L. B. F. M., & Tielens, A. G. G. M. 2014, A&A, 563, A78
Manara, C. F., Ansdell, M., Rosotti, G. P., et al. 2023, in ASP Conf. Ser. 534, Protostars and Planets VII, ed. S. Inutsuka et al. (San Francisco, CA: ASP), 539
Manara, C. F., Beccari, G., Da Rio, N., et al. 2013a, A&A, 558, A114
Manara, C. F., Fedele, D., Herczeg, G. J., & Teixeira, P. S. 2016, A&A, 585, A136
Manara, C. F., Frasca, A., Alcalá, J. M., et al. 2017a, A&A, 605, A86
Manara, C. F., Frasca, A., Venuti, L., et al. 2021, A&A, 650, A196
Manara, C. F., Mordasini, C., Testi, L., et al. 2019, A&A, 631, L2
Manara, C. F., Testi, L., Herczeg, G. J., et al. 2017b, A&A, 604, A127
Manara, C. F., Testi, L., Rigliaco, E., et al. 2013b, A&A, 551, A107
Manoj, P., Kim, K. H., Furlan, E., et al. 2011, ApJS, 193, 11
Maucó, K., Briceño, C., Calvet, N., et al. 2018, ApJ, 859, 1
McClure, M. K. 2019, A&A, 632, A32
McClure, M. K., Dominik, C., & Kama, M. 2020, A&A, 642, L15
Menu, J., van Boekel, R., Henning, T., et al. 2015, A&A, 581, A107
Meyers, J. 2015, jmeyers314/linmix, Commit: 933dbb1, GitHub, https://github.com/jmeyers314/linmix
Micolta, M., Calvet, N., Thanathibodee, T., et al. 2023, ApJ, 953, 177
Moto'oka, K., & Itoh, Y. 2013, RAA, 13, 1189
Mulders, G. D., Pascucci, I., Manara, C. F., et al. 2017, ApJ, 847, 31
Muzerolle, J., Calvet, N., & Hartmann, L. 2001, ApJ, 550, 944
Muzerolle, J., Hartmann, L., & Calvet, N. 1998, AJ, 116, 455
Neal, J., & Figueira, P. 2019, Jason-Neal/Eniric: Eniric JOSS Release, v1.0, Zenodo, doi:10.5281/zenodo.2658917
Nieva, M. F., & Przybilla, N. 2012, A&A, 539, A143
Öberg, K. I., Facchini, S., & Anderson, D. E. 2023, ARA&A, 61, 287
Paardekooper, S. J., & Mellema, G. 2006, A&A, 453, 1129
Pascucci, I., Testi, L., Herczeg, G. J., et al. 2016, ApJ, 831, 125
Pinilla, P., Birnstiel, T., Ricci, L., et al. 2012, A&A, 538, A114
Pittman, C. V., Espaillat, C. C., Robinson, C. E., et al. 2022, AJ, 164, 201
Proffitt, C. R., Roman-Duval, J., Taylor, J. M., et al. 2021, RNAAS, 5, 36
Ribas, Á., Merín, B., Bouy, H., & Maud, L. T. 2014, A&A, 561, A54
Richert, A. J. W., Getman, K. V., Feigelson, E. D., et al. 2018, MNRAS, 477, 5191
Rilinger, A. M., Espaillat, C. C., Xin, Z., et al. 2023, ApJ, 944, 66
Santos, N. C., Melo, C., James, D. J., et al. 2008, A&A, 480, 889
Savvidou, S., & Bitsch, B. 2023, A&A, 679, A42
Schegerer, A. A., Ratzka, T., Schuller, P. A., et al. 2013, A&A, 555, A103
Schneider, A. D., & Bitsch, B. 2021a, A&A, 654, A71
Schneider, A. D., & Bitsch, B. 2021b, A&A, 654, A72
Spina, L., Randich, S., Palla, F., et al. 2014, A&A, 568, A2
Stelzer, B., & Schmitt, J. H. M. M. 2004, A&A, 418, 687
Thanathibodee, T., Calvet, N., Muzerolle, J., et al. 2019, ApJ, 884, 86
Thanathibodee, T., Molina, B., Serna, J., et al. 2023, ApJ, 944, 90
Thiabaud, A., Marboeuf, U., Alibert, Y., et al. 2014, A&A, 562, A27
van der Marel, N. 2023, EPJP, 138, 225
van der Marel, N., Birnstiel, T., Garufi, A., et al. 2021, AJ, 161, 33
Vernet, J., Dekker, H., D'Odorico, S., et al. 2011, A&A, 536, A105
Virtanen, P., Gommers, R., Oliphant, T. E., et al. 2020, NatMe, 17, 261
Weidenschilling, S. J. 1997, Icar, 127, 290
Zhang, S., Zhu, Z., Huang, J., et al. 2018, ApJL, 869, L47
Zhu, Z., Nelson, R. P., Dong, R., Espaillat, C., & Hartmann, L. 2012, ApJ, 755, 6
Zhu, Z., Nelson, R. P., Hartmann, L., Espaillat, C., & Calvet, N. 2011, ApJ, 729, 47